Distribution properties of airflow in the full envelope type maize stalk chopping chamber

Peng Liu[1,6], Jin He[2*], Changchang Yu[3], Shangyi Lou[4], Chunlei Wang[5], Mingxu Wang[1], Huipeng Shen[1]

(1. *School of Electromechanical Engineering, Henan University of Technology, Zhengzhou 450001, China*;
2. *College of Engineering, China Agricultural University, Beijing 100083, China*;
3. *College of Mechanical and Electrical Engineering, Henan Agriculture University, Zhengzhou 450002, China*;
4. *School of Mechanical Engineering, Tianjin University of Technology and Education, Tianjin 300222, China*;
5. *College of Engineering and Technology, Southwest University, Chongqing 400715, China*;
6. *Henan Ancai Hi-Tech Limited Liability Company, Anyang 455000, Henan, China*)

Abstract: Chopped and spread maize stalks improve soil structure and fertility. However, because of the absence of research on airflow distribution in the chopping chamber, improvement of the spreading uniformity of chopped stalks has been limited. Therefore, in this study, computational fluid dynamics (CFD) technology was applied to analyze the influence of structural and operational parameters of the chopping and spreading machine on the velocity, pressure, and turbulent kinetic energy distribution of airflow in the chopping chamber. The experimental factors considered were the relative position angle (RPA) between the collecting-chopping shaft and the sliding-supporting shaft, working velocity (WV) of the chopping chamber, and rotational velocity of the collecting-chopping blade (RVCCB). The results revealed that RPA and RVCCB had a significant influence on the maximum negative pressure in the inlet (MNPI), the proportion of negative pressure area at inlet (PNPAI), and the maximum pressure drop at inlet and outlet (MPDIO). Additionally, RVCCB had a strong influence on the maximum velocity, average velocity, and velocity variation coefficient of airflow at the outlet. Moreover, maximum turbulence (MT) and maximum turbulent kinetic energy dissipation rate (MTKEDR) showed a positive relationship with RVCCB. To determine the values of RPA, RVCCB, and WV, a multivariate parameters optimization regression model was constructed, which yielded the optimal values of 15°, 1800 r/min, and 0.50 m/s, respectively. Subsequently, a hyperbolic spiral-type guiding shell with an arc length of 90° was designed to enhance the uniform distribution of airflow in the chopping chamber. Finally, a validation experiment of airflow distribution was conducted. The results showed that the velocity difference between the simulation and the validation experiment was less than 15%, indicating the accuracy of CFD simulation, and the spreading uniformities of the chopped stalks were better than national standards. These findings can serve as technical and theoretical support for the design and optimization of chopping and spreading machines.

Keywords: maize stalk retention, conservation tillage, spreading process, airflow distribution, full envelope-type chopping chamber

DOI: 10.25165/j.ijabe.20241705.8561

Citation: Liu P, He J, Yu C C, Lou S Y, Wang C L, Wang M X, et al. Distribution properties of airflow in the full envelope type maize stalk chopping chamber. Int J Agric & Biol Eng, 2024; 17(5): 137–150.

1 Introduction

Maize is the largest cereal crop in the world, with China being a significant producer. In 2022, China's maize planting areas and yields reached 4.31 million hm^2 and 27.72 Mt, respectively, with an estimated 41.58 Mt of maize stalks being produced[1,2]. Due to China's high-speed economic development and growing environmental concerns, the burning of maize stalks has been prohibited, leading to the need for proper disposal methods.

Maize stalks are rich in microelements, such as nitrogen, phosphorus, potassium, and organic carbon, making them an important bioresource[3,4]. The simplest way to handle maize straws is by chopping and spreading them in the field, although other methods such as utilizing them for new energy, industrial materials, and fodder also exist[5,6]. Many studies have shown the advantages of maize straw retention in the field, including improved soil structure and fertility, increased soil organic carbon content and water use efficiency, and reduced surface soil bulk density[7,8].

The crop stalks chopping and spreading machine is a key agricultural machine. However, the implementation and application of crop stalk retention have been hindered by issues related to lower uniformity in the spreading of chopped straw, such as the formation of piles and stripes[9-11]. Several research studies have focused on improving the spreading uniformity of chopped crop stalks. In terms of the design and optimization of the chopping and spreading

Received date: 2023-09-30 **Accepted date:** 2024-07-28

Biographies: Peng Liu, PhD candidate, Lecturer, research interest: conservation tillage and equipment, Email: liupeng@haut.edu.cn; **Changchang Yu**, PhD, Lecturer, research interest: conservation tillage and equipment, Email: yuchang@henau.edu.cn; **Shangyi Lou**, PhD, Lecturer, research interest: conservation tillage and equipment, Email: xxshangy1@163.com; **Chunlei Wang**, PhD, Lecturer, research interest: conservation tillage and equipment, Email: wangchunlei@swu.edu.cn; **Mingxu Wang**, PhD, Associate Professor, research interest: computational fluid dynamics simulation, Email: wmx20032002@163.com; **Huipeng Shen**, PhD, Associate Professor, research interest: computational fluid dynamics simulation, Email: hpengshen@haut.edu.cn.

***Corresponding author: Jin He**, PhD, Professor, research interest: conservation tillage technology and equipment. College of Engineering, China Agriculture University, No.17, Qinghua East Road, Haidian District, Beijing 100083, China. Tel: +86-10-62737300, Email: hejin@cau.edu.cn.

machine, Qin et al.[12], based on theoretical analysis and simulation, found that an angle of 22° for the stalk spreading plate resulted in a spreading uniformity of 88.1% and a qualified spreading rate of 90.2%. Zhang et al.[13] designed a logarithmic spiral-type chamber to enhance the spreading velocity and quality of chopped stalks, while Xu et al.[14] developed a chopped stalk guiding device that achieved a spreading uniformity of 79.8%. The kinematic analysis of chopped stalk spreading has indicated the effects of various factors such as initial velocity, mass, and moving time on the spreading area[15,16] .

In the spreading process of chopped stalks, air serves as the carrier for the chopped stalks within the chopping chamber. Therefore, the distribution of velocity, pressure, and turbulent kinetic energy of air in the chopping chamber significantly influences the motion of the chopped stalks. Numerous studies have been conducted to improve the spreading uniformity of chopped stalks. For instance, Niu et al.[17] found that a 3° angle between the blade and field surface generated more vortices above the blade head compared to other angles. Lisowski et al.[18] utilized computational fluid dynamics (CFD) technology to show that the velocity of airflow experienced abrupt changes in the boundary section. Zhang et al.[13] increased the airflow velocity at the chopping chamber outlet by installing fans in the rotational shaft, while Chen et al.[19] found relatively uniform airflow velocity distribution with three blades and a rotational velocity of 630 r/min. Sun et al.[20] observed a significant increase in airflow velocity in the chopping chamber by installing rectangular fans on the chopping blade, and Liang et al.[21] studied the effects of operation load on the velocity and pressure in a multi-duct cleaning device.

The previous research on the influence of the structure of the chopping blade, chopping chamber, and operation parameters of the chopping and spreading machine provided references for design and optimization, but mainly focused on machines with one chopping shaft. The above results provided the references for the design and optimization of chopping and spreading machines. However, the high rotational velocity of the chopping blade shaft directly affects the distribution of velocity, pressure, and turbulent kinetic energy of airflow in the chopping chamber, which ultimately impacts the spreading uniformity of chopped maize stalks. To analyze the distribution of airflow in the chopping chamber, CFD technology was used, which has been widely used in previous research on agricultural machines to analyze flow field characteristics under different operation parameters[22-24]. Therefore, the objective of this research was to determine the effect of the rotational velocity of the chopping blade, working velocity, and relative position angle on the distribution of velocity, pressure, and turbulent kinetic energy of airflow in a self-designed double rollers-type maize stalk chopping and spreading machine with different rotational velocities. The results will provide a reference for the optimization and application of stalk chopping and spreading machines.

2 Materials and methods

2.1 Structure of the maize stalk chopping and spreading machine

The self-designed double rollers-type maize stalk chopping and spreading machine with different rotational velocities in this research mainly included a collecting-chopping device, a sliding-supporting device, a transmission device, a suspension device, and a full envelope-type chopping chamber (Figure 1). The collecting-chopping device and sliding-supporting device included 40 collecting-chopping blades and 21 sliding-supporting blades, respectively. The collecting-chopping blades were arranged in a symmetrical double-helix pattern, and a sliding-supporting blade was installed between the two collecting-chopping blades. The overlap distance between the motion trail of the sliding-supporting blade and the motion trail of the collecting-chopping blade was 40 mm to achieve better cutting of stalks. The structure and arrangement of the collecting-chopping blade and sliding-supporting blade are shown in previously published theses[10, 25].

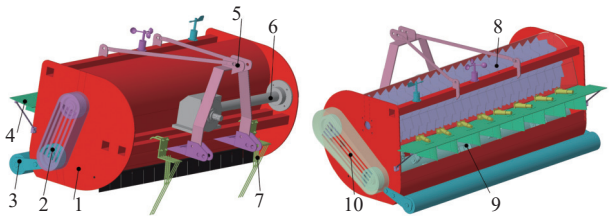

a. Axonometric drawing b. Axonometric drawing

1. Chopping chamber, 2. Decelerating device, 3. Depth-limiting device, 4. Spreading device for chopped stalk, 5. Suspension device, 6. Transmission device, 7. Provoking device for maize stalk, 8. Sliding-supporting device, 9. Collecting-chopping device, 10. Accelerating device

Figure 1 Structure of double rollers-type maize stalk chopping and spreading machine with different rotational velocities

2.2 Structure of the chopping chamber

The folded shell is always used in existing chopping and spreading machines. It has many advantages, such as easy manufacturing and lower cost, but in the bending regions of the folded shell, turbulence easily occurs, leading to the sudden change of the moving velocity and path of chopped stalks and resulting in a reduction in the spreading uniformity of chopped stalks. Therefore, to improve the distribution uniformity of airflow in the chopping chamber, a full envelope-type maize stalk chopping chamber was designed based on the double-rollers maize stalk chopping method with different rotation speeds (Figure 2). The collecting and chopping shaft and the sliding-supporting shaft were installed inside the chopping chamber. According to the relative position angle (RPA) of the two shafts, the anteverted, symmetrical, and retroverted full envelope-type chopping chamber designs were defined, with RPAs of –15°, 0°, and 15°, respectively (Figure 1).

2.3 Research on airflow distribution in full envelope-type chopping chamber

In this study, CFD analysis was used to investigate the effect of structure parameters and working velocity (WV) of chopping chamber and rotational velocity of collecting-chopping blade (RVCCB) on airflow distribution in the chopping chamber, providing references for improving the chopping and spreading quality of maize stalks.

For the airflow process in chopping chamber, the laws of conservation of energy, momentum and mass were complied. To ensure the accuracy of simulation results and improve simulation efficiency, some hypotheses were stated as followed: 1) air in the chopping chamber is a perfect gas, steady, incompressible, adiabatic, and viscous with turbulence; 2) the change of thermal conductivity, specific heat and other parameters of the medium over time and space is ignored; 3) the effect of slits and edges of the chopping chamber and chopped stalks on airflow distribution in chopping chamber is ignored; 4) the possibility of converting air mass into air energy is ignored. Therefore, the continuity equation and the momentum conservation equation were used as governing equations, and the turbulence equation was included to improve the accuracy of the simulation.

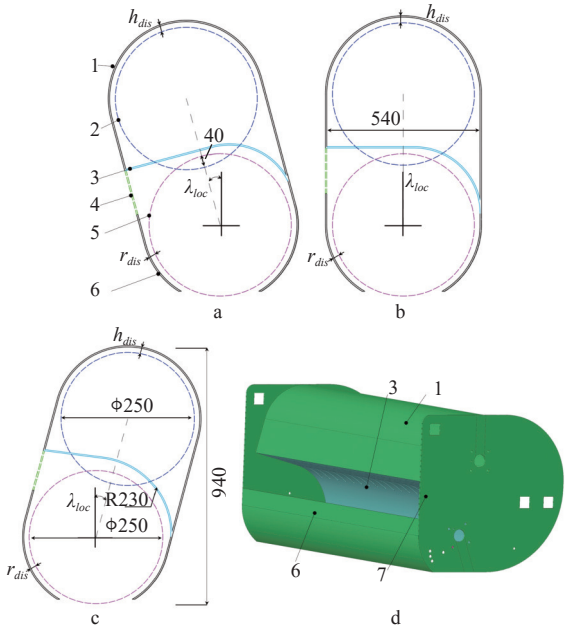

1. Front shell of chopping chamber, 2. Motion trail of sliding-supporting blade, 3. Guided flow shell for chopped stalks, 4. Outlet of chopping chamber, 5. Motion trail of collecting-chopping blade, 6. Back shell of chopping chamber, 7. Supporting plate

Note: a, b, and c represent structure diagram of retroverted, symmetrical, and anteverted full envelope-type chopping chambers, respectively; h_{dis} and r_{dis} represent the distance between the sliding-supporting blade and chopping chamber, and between the CCB and chopping chamber, which were 20 and 25 mm, respectively; d represents three-dimensional (3D) diagram of retroverted full envelope-type chopping chamber. In this figure, the units are in mm.

Figure 2 Structure diagram of full envelope-type chopping chamber

2.3.1 Fluid flow control equation

The fluid flow control equation was calculated as Equation (1):

$$\frac{\partial \rho}{\partial t} + \nabla(\rho \upsilon) = S_F \tag{1}$$

where S_F was mass source, kg/m^3; ρ was density of fluid, kg/m^3; t was the unit time, s; υ was velocity of fluid, m/s.

The momentum-conservation equation was also calculated under the rectangular coordinate system as Equation (2):

$$\frac{\partial \upsilon_i}{\partial t} + \upsilon_j \frac{\partial \upsilon_i}{\partial x_j} = -\frac{1}{\rho}\frac{\partial P}{\partial x_i} + \nu \frac{\partial}{\partial x_j}\frac{\partial \upsilon_i}{\partial x_j} + \frac{\nu}{3}\frac{\partial}{\partial x_j}\frac{\partial \upsilon_j}{\partial x_j} + F_i, \quad \nu = \frac{\mu}{\rho} \tag{2}$$

where, P is static pressure, Pa; μ was proportionality constant, constant; F_i is component of the external body force at the x_i point, N; υ_i and υ_j are the components of velocity vector in each direction, m/s; x_i and x_j are the coordinates of spatial points, m.

The renormalization group (RNG) theory k-ε turbulence model based on the Navier-Stokes (N-S) equation was used to solve the motion of fluid flow, but it is difficult to directly solve the airflow distribution in the chopping chamber by three-dimensional unsteady N-S equations[25,26]. In the stalk chopping and spreading process, the collecting-chopping blades and sliding-supporting blades with high rotational speed drove the airflow's rotation, and the motion characteristics of the airflow were turbulent. In the simulation, Reynolds time-average algorithm was used. According to the simulation classification of engineering numerical methods as given in Equation (3):

$$\frac{\partial(\rho \upsilon_i)}{\partial t} + \frac{\partial}{\partial x_i}(\rho \upsilon_i \upsilon_j) = -\frac{\partial p}{\partial x_i} + \frac{\partial \sigma_{ij}}{\partial x_j} + \frac{\partial}{\partial x_j}(-\rho \upsilon_i' \upsilon_j') \tag{3}$$

where, υ_i' is the fluctuation velocity, m/s; σ_{ij} is the component of stress tensor, Pa.

2.3.2 Pre-processing of CFD simulation

To improve simulation efficiency while ensuring calculation accuracy, the effects of certain components such as bearings, side-plates, and spacer sleeves on airflow in the chopping chamber were ignored in this study. The simplified full envelope-type chopping chamber's 3D model was transferred into Design Modeler in the ANSYS Workbench to obtain the fluid domain, which was then meshed in the Meshing module. The mesh quality of the retroverted, symmetrical, and anteverted full envelope-type chopping chambers met the simulation requirements, with mesh counts of 339 134, 339 370, and 317 844, and average grid distortions of 0.28, 0.27, and 0.29, respectively. The inlet and outlet of the chopping chamber were set as pressure inlet and pressure outlet, respectively, with a pressure of 0 Pa. The finite volume method and SIMPLE coupled algorithm were applied in this study, with a calculation step of 1.0×10^{-3} s, total steps of 2000, iteration times of 20, and total simulation time of 2 s.

A total of six planes (inlet, outlet, center plane, and planes P1 to P3) were selected to analyze the airflow distribution in different planes, as shown in Figure 3. In this analysis, considering both the quality of chopping and quality of spreading, RPA, WV, and RVCCB were set as the experimental factors based on the results of previous research[10,25] (Table 1). The experimental indices included the maximum negative pressure in the inlet (MNPI), proportion of negative pressure area at inlet (PNPAI), maximum pressure drop at inlet and outlet (MPDIO), airflow velocity variation coefficient at outlet (AVVC), maximum turbulence (MT), and maximum turbulent kinetic energy dissipation rate (MTKEDR) in different planes. In addition, the rotational velocity of the sliding-supporting shaft was half that of the collecting-chopping shaft.

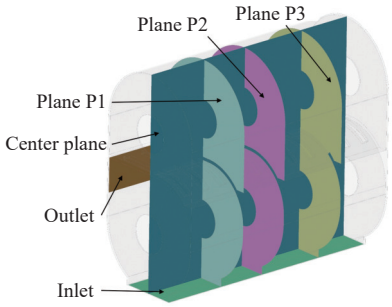

Notes: Center plane passed through the collecting-chopping shaft axis and sliding-supporting shaft axis; Plane P1 was parallel to the sliding-supporting blade, and passed through the collecting-chopping blade, and did not pass through sliding-supporting blade; Plane P2 was parallel to the sliding-supporting blade, and located between collecting-chopping blade and sliding-supporting blade; Plane P3 was parallel to sliding-supporting blade, and did not pass through the collecting-chopping blade, but passed through sliding-supporting blade.

Figure 3 Positions of selected planes (symmetrical full envelope-type chopping chamber as example)

Table 1 Levels of experimental factors

Parameters	Value
RPA/(°)	–15, 0, 15
WV/m·s^{-1}	0, 0.25, 0.50, 1.00
RVCCB/r·min^{-1}	1600, 1800, 2000, 2200, 2400

2.3.3 Field validation experiment

To verify the rationality of the chopping chamber design, a field validation experiment was conducted in the conservation

tillage experimental field in Zhuozhou Science and Technology Park of China Agricultural University National Institute for Conservation Tillage (39°28′N, 115°56′E) (Figure 4). The crop planting mode is two crops of wheat and maize a year. The average row spacing and plant spacing for maize were 610 and 198 mm, respectively. The diameter distribution of maize stalks ranged from 13.21 to 29.87 mm, with an average stalk coverage of 2.38 kg/m^2 and an average moisture content of 20.93%. The spreading uniformity of chopped stalks was measured according to the China National Standard "GB/T 24675.6-2009 Conservation tillage equipment-smashed stalk machine". The main instruments and equipment used in the experiment included a Lovol 1254 tractor, an electronic scale (accuracy: 5 g), a 1 m^2 square frame, a meter ruler, etc. Tractor working speed was 1.8 km/h, the rotational speed of collecting-chopping blade was 1600, 1800, 2000, 2200 r/min, and the rotational speed of sliding-supporting blade was half that of the collecting-chopping blade. The spreading uniformity of chopped stalks was calculated as Equation (4).

$$S_p = \frac{6\sqrt{\frac{1}{5}\sum_{i=1}^{6}\left(m_{sti}-\frac{1}{6}\sum_{i=1}^{6}m_{sti}\right)^2}}{\sum_{i=1}^{6}m_{sti}}\times 100\% \quad (4)$$

where, S_p is the spreading uniformity of chopped straw, %; m_{sti} is the mass of chopped straw at the i-th test point, kg.

Figure 4 Field validation experiment

To ensure the accuracy of simulation results, the velocities of airflow at the anteverted full envelope-type chopping chamber outlet were measured (Figure 5). The rotational velocities of the collecting-chopping blade were stabilized at 1600, 1800, 2000, and 2200 r/min, respectively, with the blade in a non-loaded state and the control accelerator of the tractor set accordingly. The velocity of airflow was measured using an impeller anemometer (China Suwei Technology Co., Ltd., velocity range: 0-45 m/s; precision: ±2.5%).

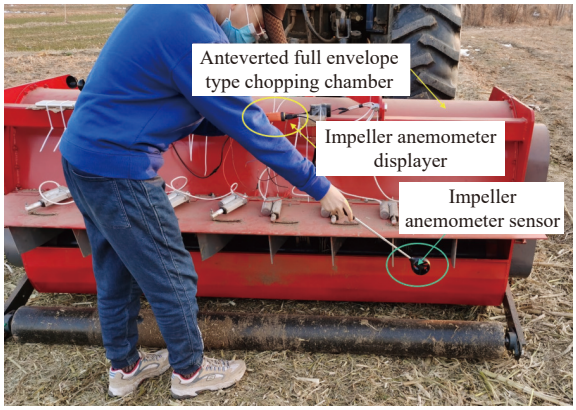

Figure 5 Measuring experiment of airflow velocity at chamber outlet

At the chopping chamber outlet, 20 measuring points were selected along two lines (L_1 and L_2), as depicted in Figure 6. The intervals in x and y-axis direction were 55 and 100 mm, respectively. Three replicate measurements were performed to calculate the mean and standard deviation of airflow velocity and compare it with the simulation results at these measuring points.

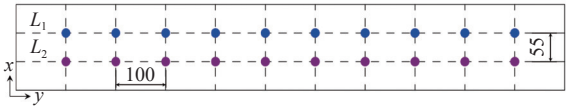

Note: The circle points represent the positions of the measuring points, mm.

Figure 6 Positions of measuring points

2.4 Data analysis

PNPAI was calculated as Equation (5):

$$\eta_{neg} = \frac{A_{neg}}{A_{tot}}\times 100\% \quad (5)$$

where, η_{neg} is the PNPAI, %; A_{neg} is the negative pressure areas at inlet, mm^2; A_{tot} is total areas of inlet, mm^2.

MPDIO was calculated as Equation (6):

$$P_{mpd} = P_{outm} - P_{inm} \quad (6)$$

where, P_{mpd} is MPDIO, Pa; P_{outm} is the maximum pressure at outlet, Pa; P_{inm} is the maximum negative pressure at inlet, Pa.

AVVC was calculated as Equation (7):

$$C_{vo} = \frac{S_{vo}}{M_{vo}}\times 100\% \quad (7)$$

where, C_{vo} is the AVVC, %; S_{vo} is the standard deviation of airflow velocity at outlet, m/s; M_{vo} is the average of airflow velocity at outlet, m/s.

3 Results and discussion

3.1 Influence analysis of pressure at inlet and outlet

3.1.1 Significance analysis

According to the significance analysis of inlet and outlet pressure, the results showed that RPA had a very significant effect on MNPI (p=0.016), and had an extremely significant effect on PNPAI and MPDIO (p<0.01); RVCCB had an extremely significant effect on MNPI and MPDIO (p<0.01), and had a very significant effect on PNPAI (p=0.047). The WV had a very significant effect on PNPAI (p=0.023). For MNPI and MPDIO, the influence levels were RVCCB>RPA>WV; for PNPAI, the influence levels were RPA>WV>RVCCB (Table 2).

Table 2 Significance analysis of inlet and outlet pressure

Parameters	MNPI		PNPAI		MPDIO	
	Chi-square	p	Chi-square	p	Chi-square	p
RPA	8.19	**	24.17	***	16.494	***
RVCCB	53.61	***	9.62	**	52.994	***
WV	1.18	n.s	11.32	**	0.360	n.s

Notes: *, **, ***, and n.s represent significant influence ($0.05\leq p<0.1$), very significant influence ($0.01\leq p<0.05$), extremely significant influence ($p<0.01$), and nonsignificant influence ($p>0.1$), respectively; Same as below.

3.1.2 Influence analysis of inlet negative pressure

In the chopping process of maize stalks, the collecting-chopping blade with high rotational velocity disturbed the airflow in the chopping chamber. Then at the inlet of the chopping chamber, the negative pressure occurred to collect maize stalks on the field surface. Therefore, MNPI was an important index to judge the

collecting ability of the chopping and spreading machine. The effects of RPA, RVCCB, and WV on MNPI are shown in Figure 7. At different RPAs and WVs, RVCCB and MNPI had a positive correlation. When RVCCB was 2400 r/min, the negative pressures at the inlet of anteverted, symmetrical, and retroverted full envelope-type chopping chambers were 244.64 Pa (RPA=15°), 161.28 Pa (RPA=0°), and 246.82 Pa (RPA=–15°), respectively. Under different RPAs, compared with RVCCB at 1600 r/min, MNPI improved by more than 105% with RVCCB at 2400 r/min. Furthermore, MNPIs initially decreased and then increased with increasing RPA, reaching the minimum value at RPA 0°, but the difference in MNPIs between RPA 15° and –15° was less than 5%. Compared to RPA 0°, MNPIs under RPA 15° increased by 15.18% (1600 r/min), 34.42% (1800 r/min), 16.28% (2000 r/min), 34.37% (2200 r/min), and 37.56% (2400 r/min).

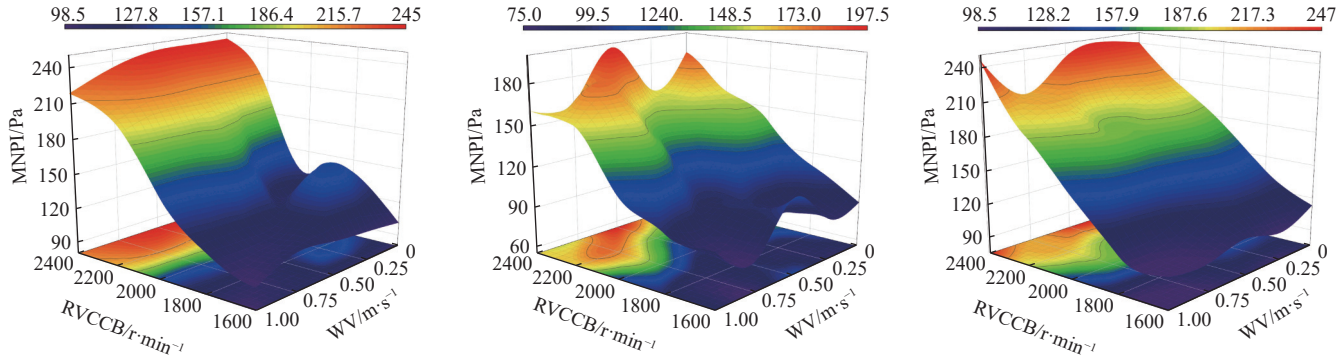

a. MNPI under RPA 15° b. MNPI under RPA 0° c. MNPI under RPA −15°

Figure 7 Effects of RPA, RVCCB, and WV on MNPI

PNPAI is an essential indicator affecting the average collecting ability of the chopping and spreading machine. The effects of RPA, RVCCB, and WV on PNPAI were examined as shown in Figure 8. As the rotational velocity of collecting-chopping blade increased, the PNPAI first decreased and then increased; especially when WV was more than 0.5 m/s, the tendency was more obvious. When RVCCB was between 1800 to 2200 r/min, a negative relationship between PNPAI and WV was observed. Additionally, the differences in maximum PNPAI were small (anteverted: 95.33%, symmetrical: 95.01%, and retroverted: 94.93%) under WV 1.0 m/s and RVCCB 1800 r/min. The minimum PNPAIs were reached under RVCCB 2000 r/min and WV 1.0 m/s, and were 83.03% (RPA=15°), 83.51% (RPA=0°), and 85.31% (RPA=0°), respectively. Although PNPAI had a negative relationship with RPA, the change in PNPAI under different RPAs was minimal. Compared with the RPA 15°, PNPAIs improved by 1.02% and 1.73% under RPA 0° and –15°, respectively.

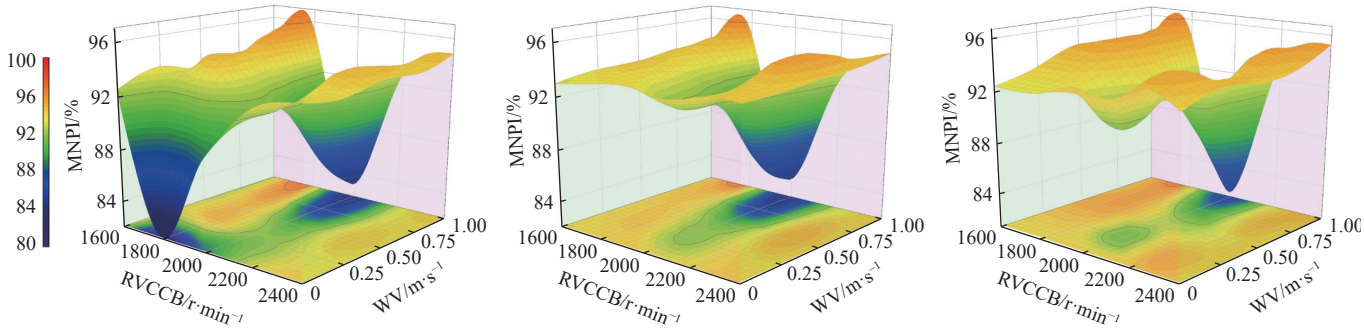

a.MNPI under RPA 15° b.MNPI under RPA 0° c.MNPI under RPA −15°

Figure 8 Effects of RPA, RVCCB, and WV on PNPAI

3.1.3 Influence analysis of MPDIO

The kinematic energy of chopped stalks was decided by the MPDIO, and the higher MPDIO helped to increase the velocity of chopped stalk existing in the chopping chamber. The effects of RPA, RVCCB, and WV on MPDIO are analyzed in Figure 9. The results indicated that MPDIO had a positive relationship with RVCCB, and the maxima of MPDIOs were reached under RVCCB 2400 r/min, which were 374.39 Pa (RPA=15°), 370.68 Pa (RPA= 0°), and 321.07 Pa (RPA= –15°). In addition, the positive effect of RPA on MPDIO was found and compared to RPA –15°; MPDIOs under RPA 15° increased by 14.46% (1600 r/min), 22.44% (1800 r/min), 11.69% (2000 r/min), 24.36% (2200 r/min), and 21.80% (2400 r/min).

3.2 Influence analysis of airflow velocity at outlet

3.2.1 Significance analysis

The maximum velocity, average velocity, and velocity variation coefficient of airflow at outlet directly affected the spreading areas and uniformity of chopped stalks. The maximum velocity and average velocity of airflow at outlet determined the maximum spreading area of chopped stalks, and the velocity variation coefficient of airflow determined the spreading uniformity of chopped stalks. Based on the analysis of variance (Table 3), RVCCB had an extremely significant effect on the maximum and average velocity of airflow (p<0.01) and a very significant effect on velocity variation coefficient of airflow (p=0.046). An extremely significant effect from WV (p<0.01) and a very significant effect from RPA (p=0.08) on velocity variation coefficient of airflow were also found.

The effects of RPA, RVCCB, and WV on maximum velocity of airflow at outlet (MVAO) are shown in Figure 10. MVAO had a positive impact with RVCCB. Compared with RVCCB at 1600 r/min, MVAOs under RPA 15°, 0°, and –15° improved by 77.46%

(0.75 m/s), 94.29% (1.00 m/s), and 110.18% (1.00 m/s), respectively. When RPA, RVCCB, and WV were 15°, 2400 r/min, and 0.75 m/s, respectively, MVAO reached a maximum (17.74 m/s). RVCCB and WV had a significant effect (p<0.1) on MVAO when RPAs were 0° and 15°, respectively, and a negative relationship between MVAO and WV was found (Table 4). Compared with WV 0 m/s, MVAOs were reduced by 17.08%/28.86% (1600 r/min), 10.94%/14.66% (1800 r/min), 14.35%/10.97% (2000 r/min), 14.03%/10.59% (2200 r/min), and –7.65%/–7.97% (2400 r/min), when RPA was 0°/–15°.

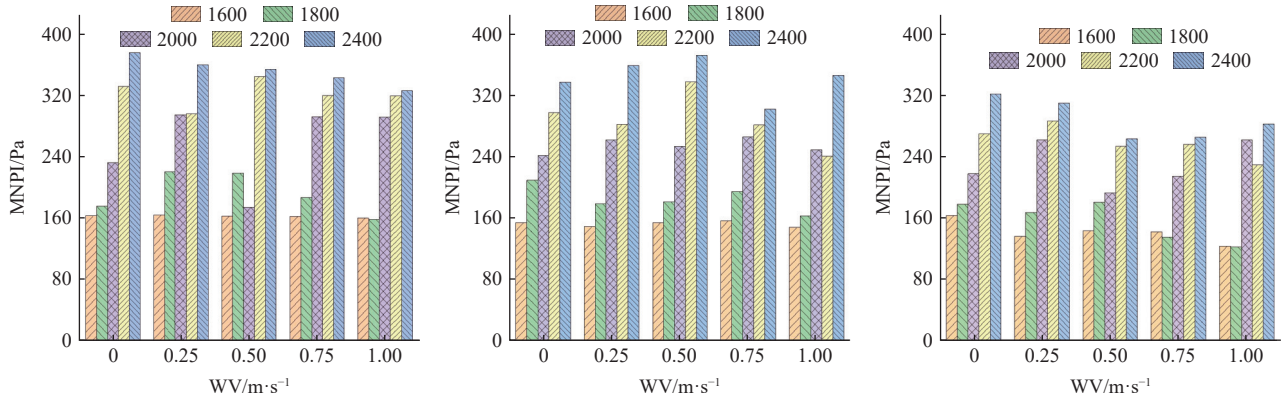

a. MNPI under RPA 15° b. MNPI under RPA 0° c. MNPI under RPA −15°

Figure 9 Effects of RPA, RVCCB, and WV on MPDIO

Table 3 Analysis of variance of airflow velocity at outlet

Parameters	RPA		WV		RVCCB	
	F	*p*	*F*	*p*	*F*	*p*
Maximum velocity airflow velocity	0.21	n.s	0.285	n.s	96.92	***
Average velocity airflow velocity	0.31	n.s	0.129	n.s	97.02	***
Velocity variation coefficient airflow velocity	2.60	*	35.452	***	2.555	**

The effects of RPA, RVCCB, and WV on average velocity of airflow at outlet (AVAO) are shown in Figure 11. Under different RPAs and WVs, AVAO increased with the increase of RVCCB. Compared with RVCCB at 1600 r/min, RPAs were improved by 51.50% (RPA=15°), 56.32% (RPA=0°), and 54.03% (RPA= –15°) under RVCCB 2400 r/min. However, no significant impacts of RPA or WV on AVAO were found (Table 4).

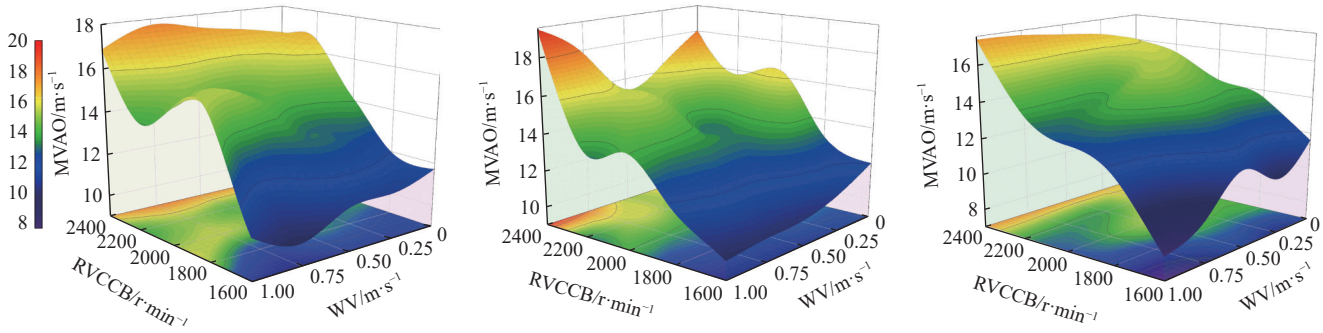

a. MNPI under RPA 15° b. MNPI under RPA 0° c. MNPI under RPA −15°

Figure 10 Effects of RPA, RVCCB, and WV on MVAO

Table 4 Analysis of variance of WV and RVCCB on MVAO

Source of variance	15°		0°		–15°	
	F	*p*	*F*	*p*	*F*	*p*
WV	0.19	n.s	2.44	**	3.32	***
RVCCB	28.53	***	33.82	***	46.25	***

The effects of RPA, RVCCB, and WV on velocity variation coefficient of airflow at outlet (VVCAO) are shown in Figure 12. A negative relationship between VVCAO and WV was indicated. Compared with WV at 0 m/s, VVCAOs were reduced by 12.50% (RPA=15°), 17.49% (RPA=0°), and 19.60% (RPA= –15°), respectively. Simultaneously, RVCCB had a positive effect on VVCAO, and when RPAs were 15°, 0°, and –15°, compared with RVCCB at 1600 r/min, VVCAOs under RVCCB at 2400 r/min were maximally increased by 13.51% (WV=0.5 m/s), 31.41% (WV=1.0 m/s), and 27.75% (WV=1.0 m/s), respectively. In addition, the result indicated that VVCAO was positively correlated with RPA, and VVCAO under RPA 15° was increased by 0.63% compared to under RPA –15°.

Based on the analysis of the pressure and velocity of airflow at inlet and outlet, the results indicated that RVCCB had a very significant effect on the pressure and velocity of airflow at the inlet and outlet. Importantly, RVCCB had a positive influence on MNPI, PNPAI, MPDIO, MVAO, AVAO, and VVCAO. The reason was that improving RVCCB directly increased the kinematic energy of airflow in the chopping chamber. Therefore, 1) improving MNPI and PNPAI was beneficial for inhaling more air and thus improving the adsorption and collecting ability of stalks by the chopping chamber; 2) the reduction of stalks rotating around the collecting-chopping shaft in the chopping chamber was achieved by improving MPDIO and airflow velocity at the outlet, which promoted the outflow of stalks in the chopping chamber and increased the spreading uniformity of stalks; 3) the kinematic energy of airflow had a positive relationship with the distance from the collecting-chopping blade due to the centrifugal motion of airflow in the chopping chamber, leading to an increase in airflow velocity above

the outlet compared to other positions, which resulted in improved VVCAO; and 4) the gradual decrease in the axial airflow velocity gradient in the chopping chamber was helpful in reducing the generation of eddy currents, which was conducive to improving the stalk spreading performance. Simultaneously, Cao et al.[27] also found that when the rotational velocity of a hammer-type chopping machine was between 2500 to 3500 r/min, the airflow velocity in the chopping chamber could be increased by about 13 m/s with every 500 r/min increase of hammer rotational velocity. In addition, improving airflow velocity at the outlet was conducive to increasing the spreading areas of chopped maize stalks, but the velocity variation coefficient of airflow also increased, leading to a deterioration in the mass uniformity of maize stalks in spreading areas. As the working velocity of the chopping and spreading machine increased, the PNPAI, MPDIO, and MNPI all decreased, but increasing RPA effectively increased the MPDIO. Zhang et al.[28] found that airflow and maximum negative pressure at the chopping chamber inlet had a negative relationship with working velocity, but installing fan-type blades on the collecting and chopping shaft effectively improved airflow and maximum negative pressure at the chopping chamber inlet.

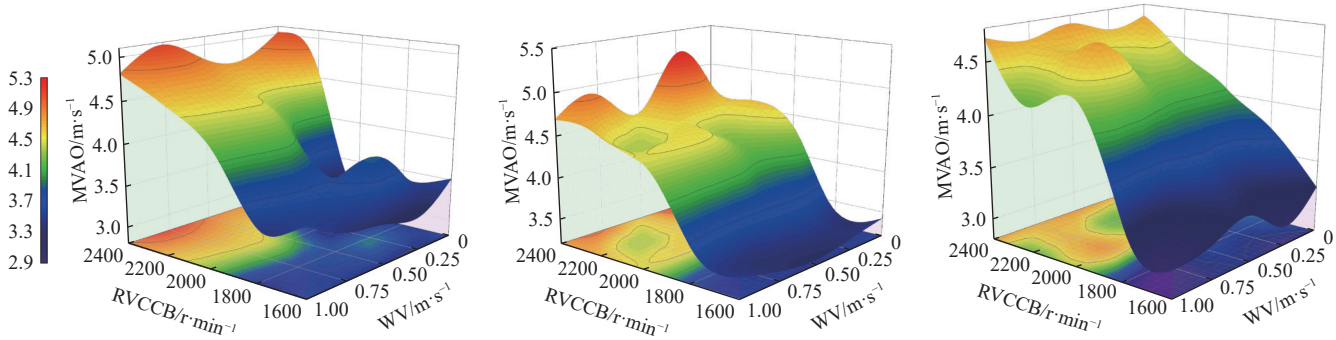

a. MNPI under RPA 15° b. MNPI under RPA 0° c. MNPI under RPA −15°

Figure 11 Effects of RPA, RVCCB, and WV on AVAO

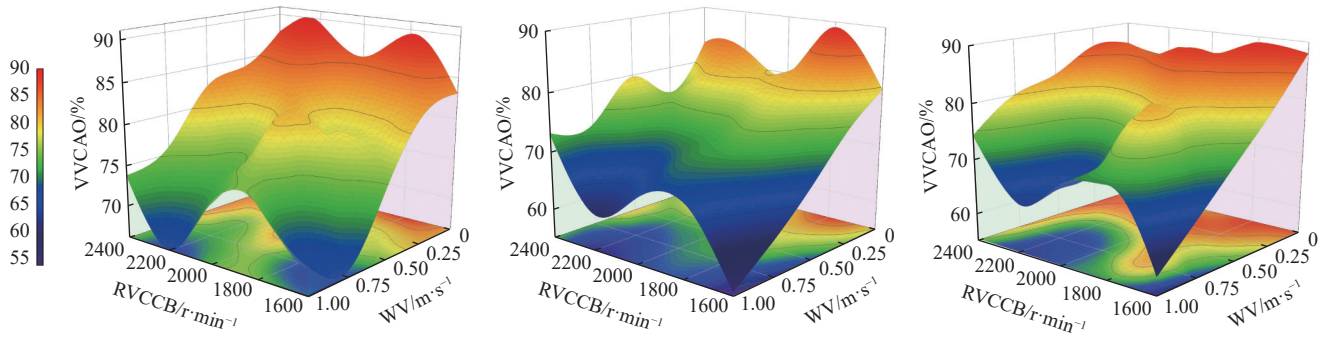

a. MNPI under RPA 15° b. MNPI under RPA 0° c. MNPI under RPA −15°

Figure 12 Effects of RPA, RVCCB, and WV on VVCAO

3.3 Influence analysis of turbulent kinetic energy and dissipation rate in chopping chamber

Turbulent kinetic energy, the key index to describe the level and development of turbulence, directly reflects the disturbance of fluid in the process of motion. Turbulent kinetic energy dissipation rate is used to judge the ability to convert gas flow kinetic energy into heat energy under molecular viscosity, and is also the rate of energy dissipation in the process of large vortex splitting into small vortex and large bubble splitting into small bubble. The greater the dissipation rate of turbulent kinetic energy, the more intense the movement in the airflow field[29]. Therefore, the higher turbulent kinetic energy and dissipation rate damaged the spreading uniformity of chopped maize stalks.

The effects of RPA, RVCCB, and WV on maximum turbulent kinetic energy of airflow (MTKEA) are shown in Figure 13. In different planes, the RVCCB had a positive effect on MTKEA, and compared with RPA and WV, RVCCB had the greatest influence on the MTKEA (Table 5). In the chopping chamber, compared with RVCCB 1600 r/min, MTKEAs were maximally increased by 125.89% (RPA=15°), 124.56% (RPA=0°), and 131.38% (RPA= –15°) under RVCCB 2400 r/min, respectively. In addition, the results indicated that the effect of WV on MTKEA was limited. Under the different RPAs, the fluctuation ranges of MTKEAs were 3.93 to 31.17 m²/s² (RPA =15°), 3.24 to 10.25 m²/s² (RPA =0°), and 2.59 to 12.48 m²/s² (RPA =–15°), respectively. The relationships between WV and MTKEA were different in different planes. For example, in the P2 and P3 planes, a positive relationship between MTKEA and RPA was found, and MTKEA under RPA –15° reached minimum values of 4.24 and 7.27 m²/s², respectively.

Table 5 Regression model of MTKEA in different planes

Model	Center plane (R^2=0.72)			Plane P1 (R^2=0.29)		
	Coefficient	*T*	*p*	Coefficient	*T*	*p*
Intercept	–5.839	–5.506	***	–3.492	–1.357	n.s
RPA	–0.015	–1.287	n.s	0.015	0.505	n.s
RVCCB	0.007	13.465	***	0.006	5.049	***
WV	0.360	0.874	n.s	–1.696	–1.696	*
	Plane P2 (R^2=0.95)			Plane P3 (R^2=0.98)		
Intercept	–3.689	–11.871	***	–4.430	–22.330	***
RPA	0.070	19.999	***	0.023	10.359	***
RVCCB	0.004	28.565	***	0.005	56.106	***
WV	0.331	2.745	***	–0.403	–5.231	***

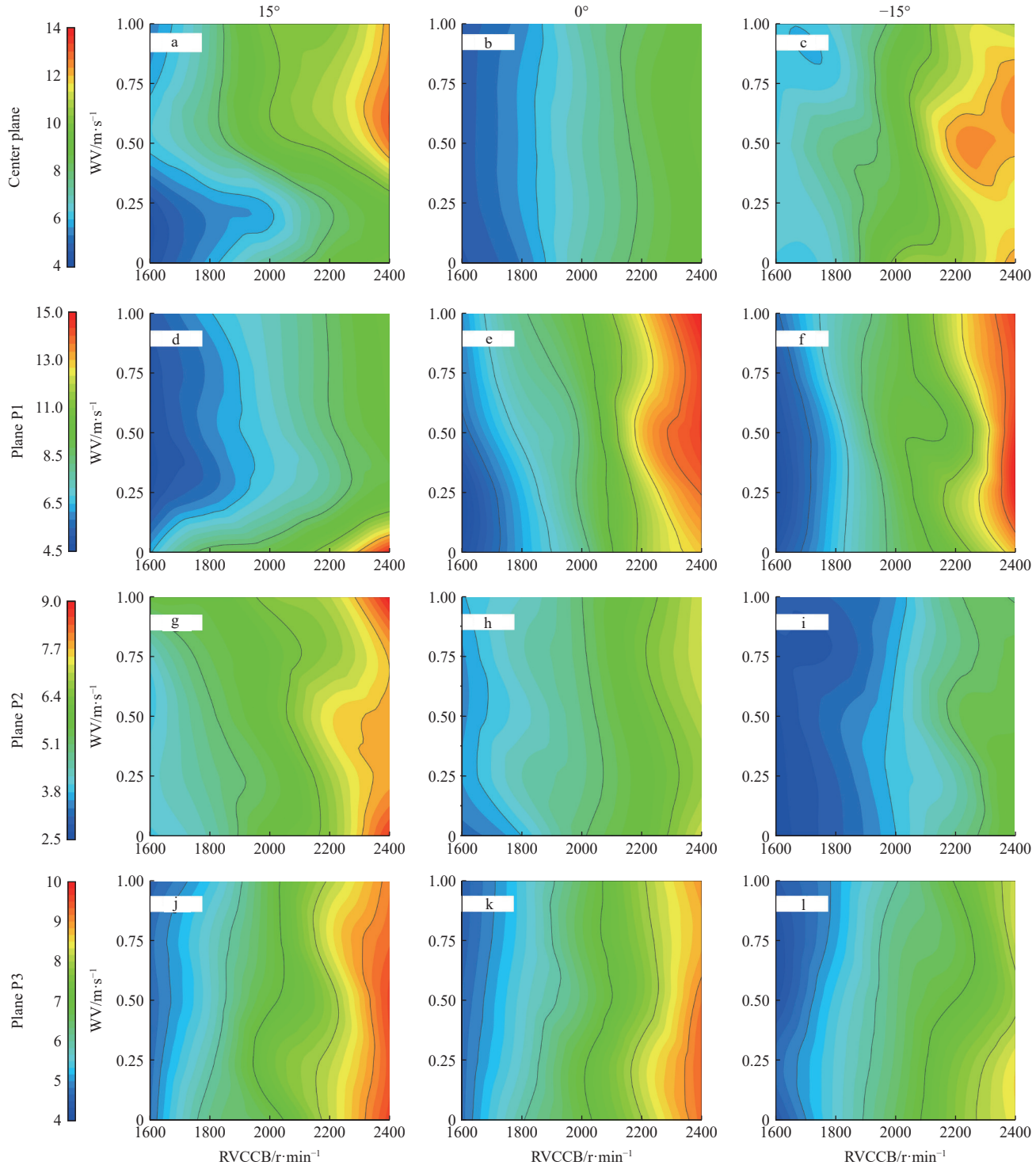

Note: a, b, and c represent the MTKEA under RPA 15°, 0°, and –15° at center plane, respectively; d, e, and f represent the MTKEA under RPA 15°, 0°, and –15° at P1 plane, respectively; g, h, and i represent the MTKEA under RPA 15°, 0°, and –15° at P2 plane, respectively; j, k, and l represent the MTKEA under RPA 15°, 0°, and –15° at P3 plane, respectively.

Figure 13 Effects of RPA, RVCCB, and WV on MTKEA

The effects of RPA, RVCCB, and WV on maximum turbulent kinetic energy dissipation rate of the airflow (MTKEDRA) are shown in Figure 14. In different planes, RVCCB had a positive effect on MTKEDRA, with the influence level being RVCCB>RPA>WV (Table 6). Compared with RVCCB 1600 r/min, MTKEDRAs were maximumly increased by 216.46% (RPA=15°), 241.83% (RPA=0°), and 220.17% (RPA=–15°) under RVCCB 2400 r/min. In the center plane and P3 plane, MTKEDRA had a negative relationship with RPA, reaching the minimum value under RPA 15°, but an insignificant effect of WV on MTKEDRA was also found.

In the double rollers maize stalk chopping machine, the components of turbulence had multiple scales. In the turbulence, larger eddies dominate the momentum transformation, and smaller eddies mainly transfer the turbulent kinetic energy into the system internal energy. In the plane of center P1, P2, and P3, RVCCB had a positive impact on MTKEA and MTKEDRA, and in the positions with larger MTKEA, the MTKEDRA also was higher than in other

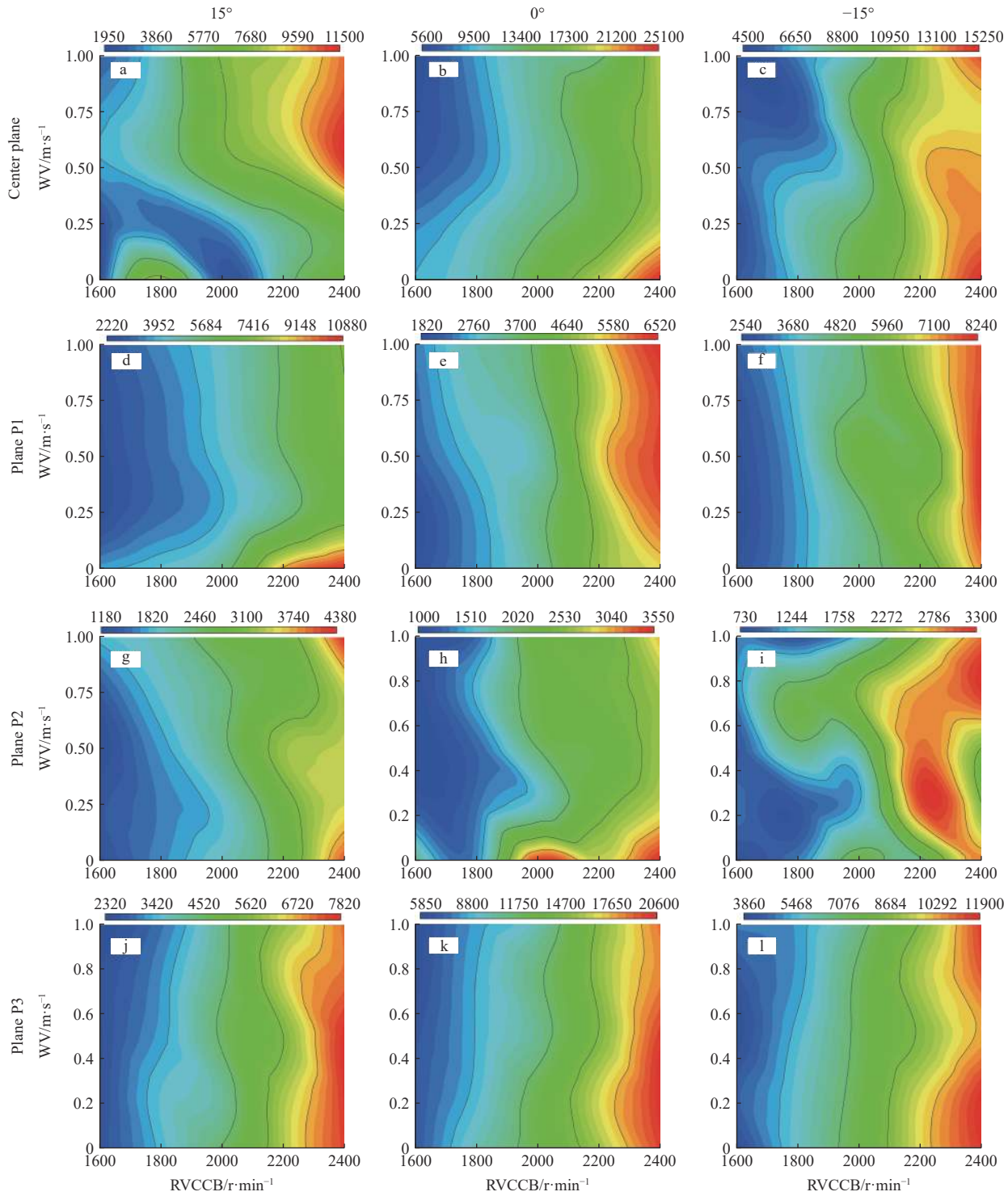

Note: a, b, and c represent the MTKEDRA under RPA 15°, 0°, and –15° at center plane, respectively; d, e, and f represent the MTKEDRA under RPA 15°, 0°, and –15° at P1 plane, respectively; g, h, and i represent the MTKEDRA under RPA 15°, 0°, and –15° at P2 plane, respectively; j, k, and l represent the MTKEDRA under RPA 15°, 0°, and –15° at P3 plane, respectively.

Figure 14 Effects of RPA, RVCCB, and WV on MTKEDRA

positions. Those results indicated that the energy dissipation of the mean flow of airflow and the turbulent kinetic energy dissipation were significant. In the chopping process of maize stalks, when the turbulent kinetic energy and dissipation rate in the chopping chamber improved, the number of smaller eddies directly promoted the collision between chopped stalks. This directly decreased the kinetic energy increase of chopped maize stalks by airflow and increased the heat energy of airflow, leading to a decrease in the spreading uniformity of chopped maize stalks and energy use efficiency[30,31].

3.4 Parameter optimization of full envelope-type chopping chamber

To indicate the influence of RPA, RVCCB, and WV on airflow field distribution, based on regression analysis, RPA, RVCCB, and WV were the independent variables; the maximum and average velocity of airflow at the outlet, MPDIO, and MNPI were the dependent variables; and the multivariate parameters model was obtained as Equation (8):

Table 6 Regression model of MTKEDRA in different planes

Model	Center plane (R^2=0.56)			Plane P1 (R^2=0.79)		
	Coefficient	T	P	Coefficient	T	P
Intercept	–13 540.36	–4.98	***	–7181.18	–9.56	***
RPA	–106.67	–3.50	***	0.86	0.10	n.s
RVCCB	11.67	8.84	***	5.95	16.30	***
WV	–681.73	–0.65	n.s	–100.83	–0.35	n.s
	Plane P2 (R^2=0.79)			Plane P3 (R^2=0.49)		
Intercept	–2968.34	–8.78	***	–12 362.22	–4.42	***
RPA	19.99	5.28	***	–94.52	–3.01	***
RVCCB	2.53	15.41	***	10.49	7.73	***
WV	59.69	0.46	n.s	–755.15	–0.70	n.s

$$\begin{bmatrix} y_1 \\ y_2 \\ y_3 \\ y_4 \end{bmatrix} = \begin{bmatrix} -0.2 \\ 0.03 \\ 3.6 \\ -0.2 \end{bmatrix} \times 10^3 - \begin{bmatrix} -9.7 \\ 1.2 \\ 9.9 \\ 4.3 \end{bmatrix} x_1 \times 10^3 + \begin{bmatrix} 0.3 \\ -0.1 \\ -5.7 \\ 0.4 \end{bmatrix} x_2 + \begin{bmatrix} -3.5 \\ -0.7 \\ 32.4 \\ -22.9 \end{bmatrix} x_3 + \begin{bmatrix} 0.01 \\ -0.1 \\ -3.5 \\ 0.88 \end{bmatrix} x_1^2 \times 10^{-2} + \begin{bmatrix} -0.2 \\ 0.02 \\ 3.0 \\ -0.2 \end{bmatrix} x_2^2 \times 10^{-3} - \begin{bmatrix} -5.8 \\ -2.0 \\ 110.7 \\ -74.7 \end{bmatrix} x_3^2 + \begin{bmatrix} -43 \\ 52.3 \\ 43.9 \\ 19.1 \end{bmatrix} x_1^3 - \begin{bmatrix} -0.2 \\ 0.04 \\ 4.9 \\ -0.4 \end{bmatrix} x_2^3 \times 10^{-7} - \begin{bmatrix} 3.1 \\ 1.3 \\ -62 \\ 52.8 \end{bmatrix} x_3^3 \quad (8)$$

where x_1, x_2, and x_3 represent the RPA, RVCCB, and WV, respectively; y_1, y_2, y_3, and y_4 represent the maximum and average velocity of airflow at outlet, MPDIO, and MNPI, respectively; and the R^2 of y_1, y_2, y_3, and y_4 are 0.86, 0.86, 0.89, and 0.88, which illustrated good function fitting effect.

To find better parameters for the full envelope-type chopping chamber, the objective function and constraint conditions were as Equation (9), and then RPA, RVCCB, and WV were calculated as 13.88°, 1865.26 r/min, and 0.53 m/s. For the manufacture of the machine and field experiment, the values were rounded off to 15°, 1800 r/min, and 0.50 m/s, and anteverted full envelope-type chopping chamber was applied.

$$\begin{cases} \max(y_1, y_2, y_3, y_4) \\ \text{s.t.} \begin{cases} -15 \le x_1 \le 15 \\ 1600 \le x_2 \le 2400 \\ 0.25 \le x_3 \le 1.0 \end{cases} \end{cases} \quad (9)$$

3.5 Influence analysis of structure of hyperbolic spiral-type guided shell on distribution of airflow

3.5.1 Structure of hyperbolic spiral-type guided shell

According to the above conclusions, anteverted full envelope-type chopping chamber was selected in this study. In the chopping chamber, airflow and chopped stalks rotated around the collecting-chopping shaft and sliding-supporting shaft by a collecting-chopping blade with high rotational velocity. If the guided shell in the chopping chamber was not installed, most of the chopped maize stalks moved around the inner edge of the chopping chamber and the collecting-chopping shaft and sliding-supporting shaft, and a small amount of chopped maize stalks were spread out of the chopping chamber, which directly affected the spreading uniformity of the chopped stalks. Importantly, the guided shell in the chopping chamber changed the movement direction of chopped maize stalks and airflow, which improved the distribution and spreading uniformity of chopped stalks. Therefore, the structure of the guided shell directly affected the distribution character of airflow in the chopping chamber and the spreading uniformity of the chopped maize stalks.

To reduce the motion resistance of the guided shell to airflow, the structure of the guided shell needed to be smooth and continuous. Therefore, hyperbolic spiral was used, and the parameter equation was calculated as Equation (10):

$$\begin{cases} x_{cs} = \dfrac{R\cos\sigma_y}{\sigma_y} \\ y_{cs} = \dfrac{R\sin\sigma_y}{\sigma_y} \end{cases} (\sigma_y \ne 0) \quad (10)$$

where x_{cs} and y_{cs} are coordinates of the culm drainage hood on the x and y axes, respectively, mm; R is the initial radius of the guided shell, mm; and σ_y is the angle between the point in the hyperbolic spiral and the x axis, (°). To improve the smoothing character of the guided shell, R is set as 550 mm.

Because of the interactive relationship between the arc length of the hyperbolic spiral-type guided shell and airflow motion, too long of an arc length was conducive to the rotational motion of the airflow in the chopping chamber, but was disadvantageous to airflow and to outflow of the chopped stalks from the chopping chamber outlet. Too short of an arc length was conducive to airflow and to outflow of the chopped stalks from the chopping chamber outlet, but the diversion effect of the guided shell on the airflow in the chopping chamber was weakened, ultimately affecting the spreading uniformity of maize stalks. To find the suitable arc length, the center of the collecting-chopping shaft was taken as the coordinate origin to establish the xOy coordinate system. Four arc lengths of the hyperbolic spiral-type guided shell were selected, and those arc lengths corresponded to the center angles (CA) of 75°, 90°, 105°, and 120°, respectively (Figure 15).

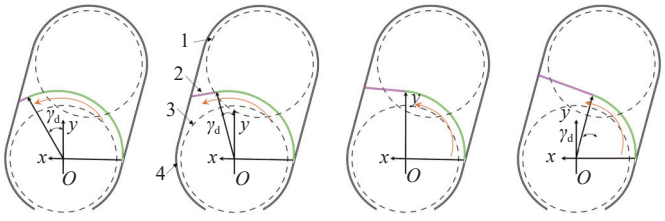

a. γ_d=30° b. γ_d=15° c. γ_d=0° d. γ_d=–15°

1. Sliding-supporting blade, 2. Hyperbolic spiral-type guided shell, 3. Collecting-chopping blade, 4. Anteverted full envelope-type chopping chamber.

Note: Green line is the hyperbolic spiral, pink line is the tangent at the end of the hyperbolic spiral, and orange line represents the motion direction of chopped straw and airflow.

Figure 15 Structure diagram of anteverted full envelope-type chopping chamber

In the chopping process of the maize stalks, the sliding-supporting blade needs to pass through the hyperbolic spiral-type guided shell and form a dynamic double supporting state for maize stalks combined with the collecting-chopping blade. To avoid interference between the sliding-supporting blade and the guided shell, the opening width and length of the guided shell were 30 and 385 mm, respectively (Figure 16).

3.5.2 Effect of arc length of hyperbolic-type guided shell on distribution of airflow

To obtain a better arc length of hyperbolic-type guided shell, the effects of arc length on airflow distribution in the chopping chamber were studied to improve the airflow distribution uniformity and spreading quality of chopped stalks. In this simulation, the

rotational velocities of the collecting-chopping blade and sliding-supporting blade were 1800 and 900 r/min, respectively, and the rotational direction was the same.

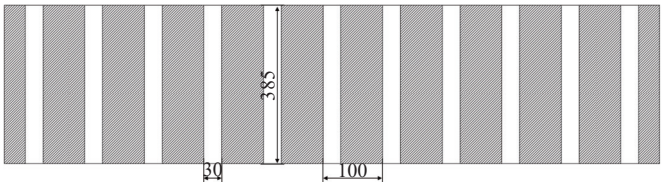

Figure 16 Top view figure of the opening location in the hyperbolic spiral-type guided shell (mm)

The pressure distribution at the chopping chamber inlet under different guided shell arc lengths is shown in Figure 17. The negative pressure at the chopping chamber inlet occurred by collecting-chopping blades with high rotational velocity, which was conducive to collecting and chopping the stalks in the field. Additionally, because in the double rollers maize stalk chopping machine the collecting-chopping blades were installed in a double helix on the shaft, and only part of the collecting-chopping blades worked on the fluid domain at the chopping chamber inlet, the uneven distribution of negative pressure at the chopping chamber inlet was indicated. Under different CAs of the guided shell, the size of the maximum negative pressure area at the chopping chamber inlet (blue region in Figure 14) was CA 105°> CA 90°> CA 120°> CA 75°. These results indicated that the larger negative pressure area at the chopping chamber inlet under CA 105° and 90° was conducive to forming a bigger pressure difference and improving the collecting and adsorbing ability for maize stalks in the field.

The distribution of velocity, pressure, and turbulent kinetic energy on the center plane is shown in Figure 18. For the hyperbolic spiral-type guided shell with different CAs, the pressure on the center plane increased radially and gradually along the axis of the collecting-chopping shaft, but the change of pressure along the

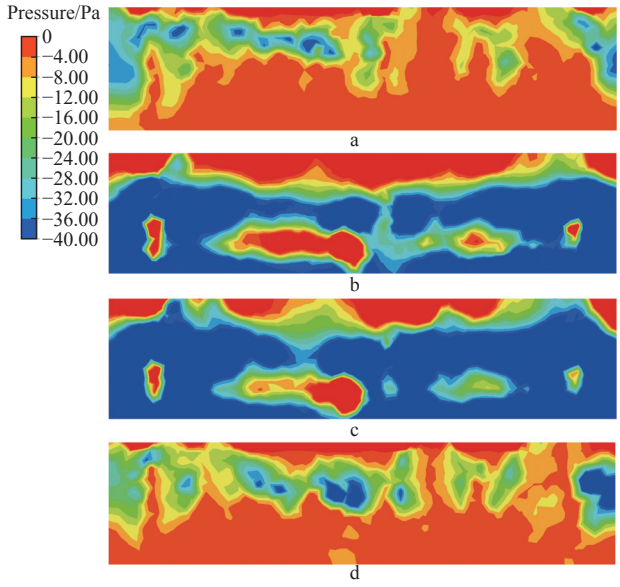

Note: a, b, c, and d represent pressure distribution under CA 75°, 90°, 105°, and 120°, respectively.

Figure 17 Pressure distribution cloud map of chopping chamber inlet

radial direction of the sliding-supporting shaft was ignored. This was due to the velocity of the collecting-chopping shaft being larger than the velocity of the sliding-supporting shaft. Near the collecting-chopping shaft, the maximum negative pressure areas under CA 105° and 120° were larger than those under CA 75° and 90°. Furthermore, the airflow velocity near the end of the collecting-chopping blade was higher than the airflow velocity in other regions, and increasing CA was conducive to improving the velocity and pressure of airflow near the end of the collecting-chopping blade to increase the kinetic energy of chopped maize

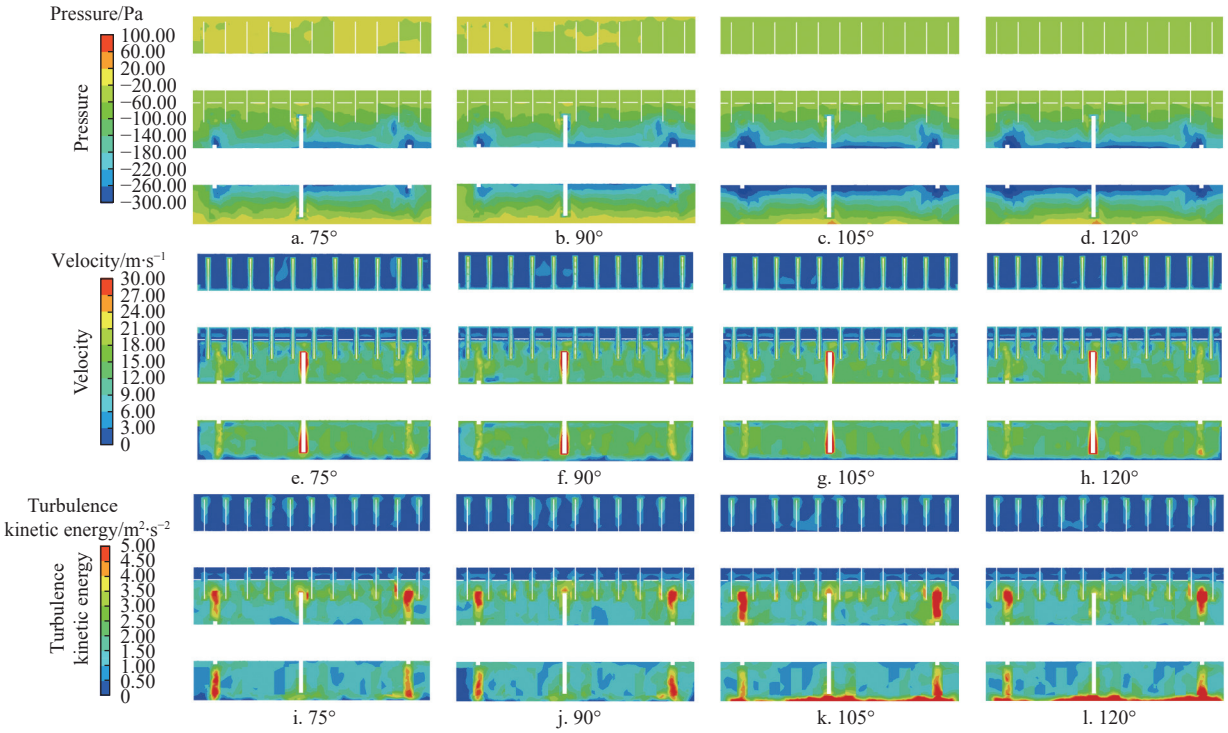

Note: a, b, c, and d represent the pressure distribution under CA 75°, 90°, 105°, and 120°, respectively; e, f, g, and h represent the velocity distribution under CA 75°, 90°, 105°, and 120°, respectively; i, j, k, and l represent the turbulent kinetic energy distribution under CA 75°, 90°, 105°, and 120°, respectively.

Figure 18 Distribution cloud map of velocity, pressure, and turbulent kinetic energy in center plane

stalks. Because of the separation influence of the guided shell on the chopping chamber, lower velocity and less disturbance of airflow on the guided shell were found. Simultaneously, in the airflow areas with large velocities and pressures, turbulent kinetic energy was also large, but reducing CA was beneficial for reducing the area and intensity of turbulent kinetic energy, reducing the number of small vortices and kinetic energy loss of chopped maize stalks, and finally increasing the spreading uniformity of chopped maize stalks.

The distribution of velocity, pressure, and turbulent kinetic energy on the plane P1 is shown in Figure 19. The results demonstrated that the pressure on the windward side of the collecting-chopping blade was higher than that of the nearby air domain, while the pressure on the leeside of the blade was lower. Additionally, airflow velocity near the end of the collecting-chopping blade exceeded that of the other regions. The pressure and velocity distribution under the guided shell in the plane P1 exhibited a positive relationship with CA. This was due to the increase in CA resulting in an increase in the arc length of the hyperbolic spiral, thereby enhancing the axial airflow in the chopping chamber around the collecting-chopping shaft. However, the elongation of the hyperbolic spiral directly caused the corn stalk to rotate around the collecting-chopping shaft, hindering its exit from the chopping chamber. Moreover, CA was positively correlated with the distribution area of turbulent kinetic energy in the chopping chamber inlet. Turbulent kinetic energy on the leeside of the chopping-collecting blade exceeded that of other airflow regions, and with an increase in CA, the turbulent kinetic energy on the leeside also increased. This, however, was detrimental to improving the spreading uniformity of chopped maize stalks.

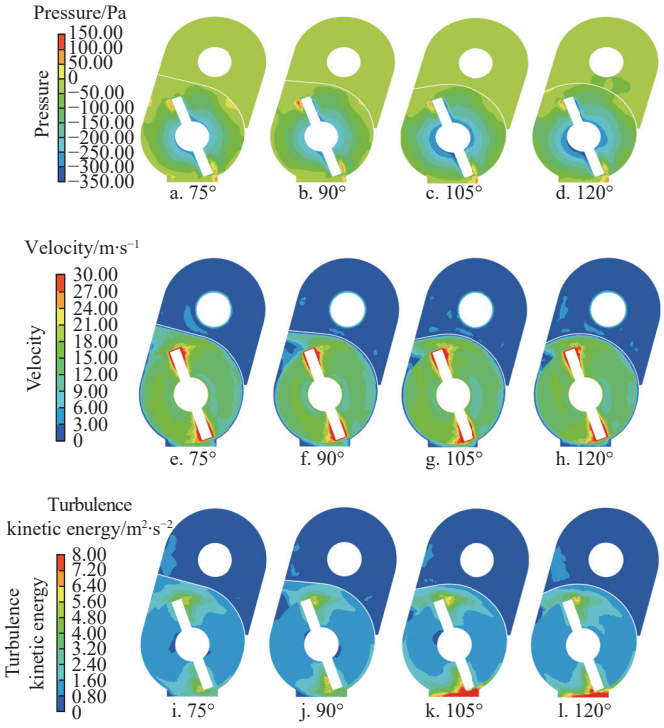

Note: a, b, c, and d represent the pressure distribution under CA 75°, 90°, 105°, and 120°, respectively; e, f, g, and h represent the velocity distribution under CA 75°, 90°, 105°, and 120°, respectively; i, j, k, and l represent the turbulent kinetic energy distribution under CA 75°, 90°, 105°, and 120°, respectively.

Figure 19 Distribution cloud map of velocity, pressure, and turbulent kinetic energy in plane P1

The distribution of velocity, pressure, and turbulent kinetic energy on plane P2 is shown in Figure 20. As the radius direction of the collecting-chopping shaft increased, there was a gradual increase in the pressure and velocity of airflow. In addition, CA negatively related to velocity of airflow at the chopping chamber outlet and the pressure of airflow in the chopping chamber, and the change in the airflow pressure on the upper and lower sides of the guided shell was ignored. Turbulent kinetic energy was primarily concentrated at the chopping chamber inlet and outlet with CA values of 105° and 120°, surpassing the levels observed at 75° and 90°. This observation indicated that vortexes were more likely to form at the inlet and outlet of the chopping chamber, thus compromising the uniformity of chopped maize stalks.

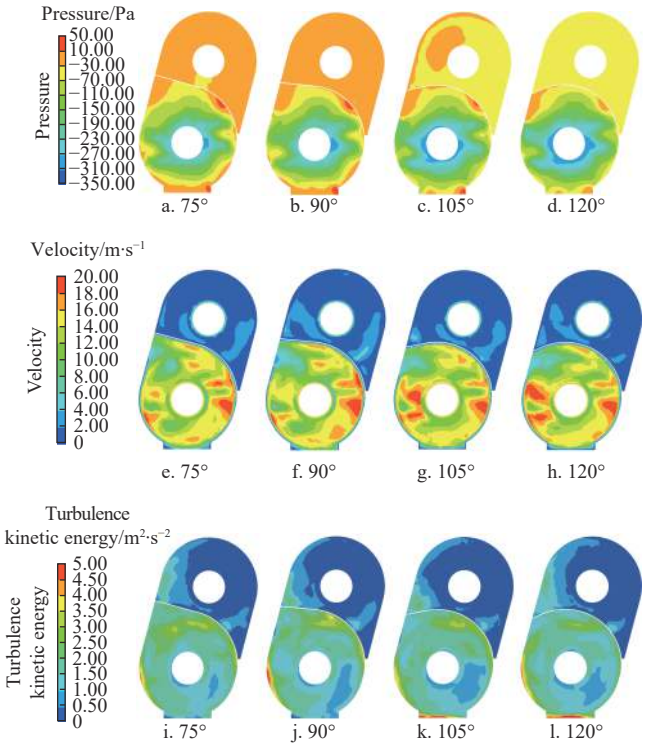

Note: a, b, c, and d represent the pressure distribution under CA 75°, 90°, 105°, and 120°, respectively; e, f, g, and h represent the velocity distribution under CA 75°, 90°, 105°, and 120°, respectively; i, j, k, and l represent the turbulent kinetic energy distribution under CA 75°, 90°, 105°, and 120°, respectively.

Figure 20 Distribution cloud map of velocity, pressure, and turbulent kinetic energy in plane P2

3.6 Validation experiment of airflow distribution in the chopping chamber

The results of the measuring and simulation at L_1 and L_2 in the chamber outlet are presented in Figure 21. According to the CFD simulation results, when RVCCBs were 1600, 1800, 2000, and 2200 r/min, the maximum/average airflow velocities at L_1 were 9.45/3.72, 11.43/4.06, 12.09/4.62, and 11.40/5.23 m/s, respectively. Similarly, the maximum/average airflow velocities at L_2 were 8.67/3.47, 10.14/4.14, 12.47/4.66, and 12.20/4.88 m/s for the same RVCCB settings. The measuring results showed that the maximum and average airflow velocities at L_1/L_2 were 3.43/3.15, 4.21/3.98, 4.76/4.15, and 5.35/4.74 m/s, respectively, when RVCCBs were 1600, 1800, 2000, and 2200 r/min. Furthermore, the spreading uniformity of chopped stalks was 79.89%, 81.76%, 82.64%, and 83.78%, when RVCCBs were 1600, 1800, 2000, and 2200 r/min, respectively, which were all superior to national standards.

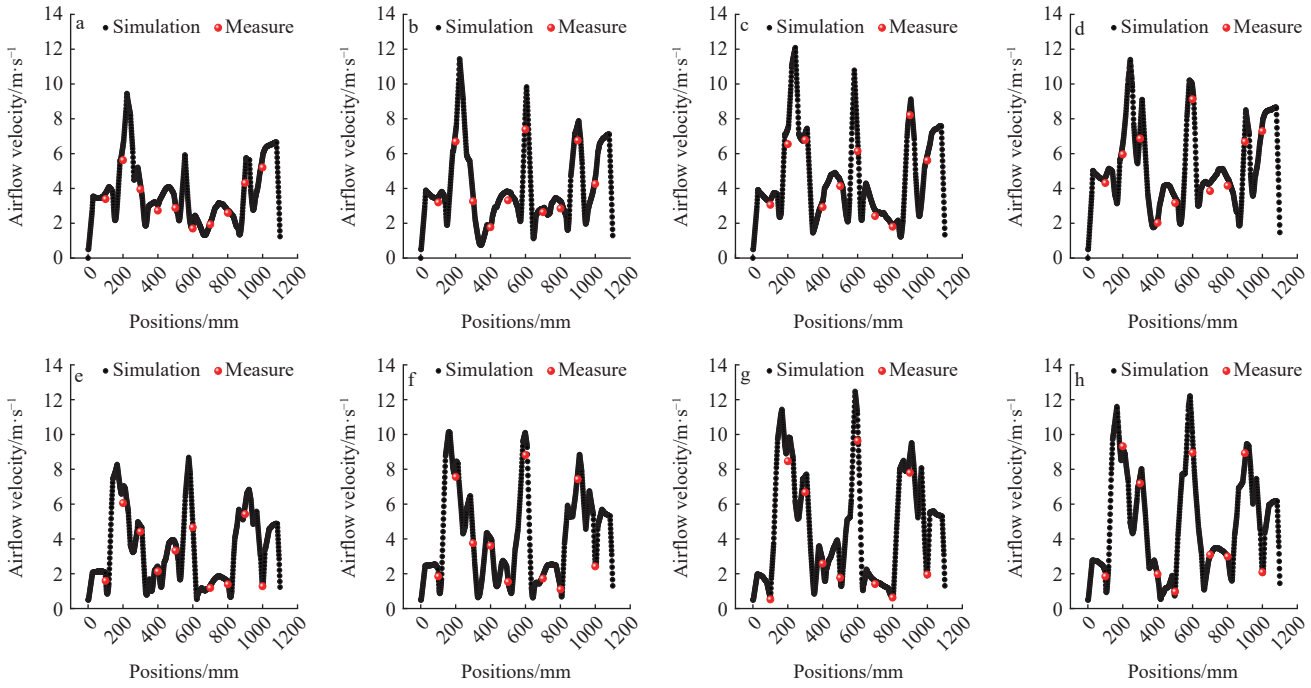

Note: a, b, c, and d represent the airflow velocity at line L_1 when RVCCBs are 1600, 1800, 2000, and 2200 r/min, respectively; e, f, g, and h represent the airflow velocity at line L_2 when RVCCBs are 1600, 1800, 2000, and 2200 r/min, respectively.

Figure 21 Comparison of airflow velocity between simulation and measuring at lines L_1 and L_2 in chamber outlet

The difference in average airflow velocity between simulation and measure at measuring points in L_1 and L_2 was less than 15%. Although the same trend of airflow velocity between simulation and measure at 20 measuring points in the chamber outlet was found, a miss distance also existed. The reasons for these discrepancies are attributed to the following: 1) the rotational velocity of the collecting-chopping blade was controlled by accelerator, so the rotational velocity could not maintain discrepancy consistently; 2) machining and installation error for the anteverted full envelope-type chopping chamber existed in the manufacture process; and 3) the impeller anemometer was not perfectly aligned vertically with the flow direction of air at the chamber outlet. Despite these reasons, the difference of airflow between simulation and measurement (less than 15%) also demonstrates the accuracy of the simulation results, which can provide a reference for the design and optimization of the full envelope-type chopping chamber.

4 Conclusions

This study investigated the effects of the structure and operation parameters of a full envelope-type chopping chamber on airflow distortion based on CFD technology. The simulation results were validated by field validation experiment. The main conclusions were as follows:

1) RVCCB had a positive relationship with MNPI, MPDIO, average velocity, velocity variation coefficient of airflow at outlet, MTKEA, and MTKEDRA; the velocity variation coefficient of airflow at outlet increased with RPA but decreased with WV; and MNPI reached its minimum under RPA 0°.

2) A multivariate parameters optimization regression model was developed for RPA, RVCCB, and WV in relation to the maximum and average velocity of airflow at the outlet, MPDIO, and MNPI. The regression model was then solved, determining the values of RPA, RVCCB, and WV at 15°, 1800 r/min, and 0.50 m/s.

3) To improve the uniform distribution of airflow in the chopping chamber, a hyperbolic spiral-type guided shell was designed; based on the analysis of the influence of the structure of the hyperbolic spiral-type guided shell on the distribution of airflow, the arc angle of hyperbolic-type guided shell was determined at 90°.

4) The validation experiment showed that the spreading uniformities of the chopped stalks were better than national standards, and the velocity difference between simulation and validation experiment was less than 15%, which indicated the accuracy of CFD simulation results.

The results of this study can provide a technical reference for design and optimization of the chopping and spreading machine. However, this study focused only on the airflow distribution; in the future, the interaction between airflow and chopped stalks needs further research.

Acknowledgements

This research was supported by Natural Science Foundation of Henan Province (Grant No. 242300421560), Science and Technology Research Project of Henan (Grant No. 232102110273), the Scientific Research Foundation for Advanced Talents of Henan University of Technology (Grant No. 2022BS077), Training Plan of Young Backbone Teachers in Colleges and Universities in Henan Province (Grant No. 2020GGJS088), and the Cultivation Programme for Young Backbone Teachers in Henan University of Technology (Grant No. 0503/21420191).

[References]

[1] National Bureau of Statistics. Agriculture, 2023. Available: https://data.stats.gov.cn/easyquery.htm?cn=C01. Accessed on [2023-08-12].

[2] Huo L L, Zhao L X, Yao Z L, Jia J X, Zhao Y N, Fu G H, Cong H B. Difference of the ratio of maize stovers to grain and spatiotemporal variation characteristics of maize stovers in China. Transactions of the CSAE, 2020; 36(21): 227–234. (in Chinese)

[3] Soltangheisi A, Haygarth P M, Pavinato P S, Cherubin M R, Teles A P B, Bordonal R D O, Carvalho J L N, Withers P J A, Martinelli LA. Long term sugarcane straw removal affects soil phosphorus dynamics. Soil Tillage

Research, 2021; 208: 104898.
[4] Zheng L, Pei J, Jin X, Schaeffer S, An T, Wang J. Impact of plastic film mulching and fertilizers on the distribution of straw-derived nitrogen in a soil-plant system based on 15 N-labeling. Geoderma, 2018; 317: 15–22.
[5] Yesufu J, Mccalmont J P, John C. C, Prysor W, John H, James G, David S. Consequential life cycle assessment of miscanthus livestock bedding, diverting straw to bioelectricity generation. GCB Bioenergy, 2020; 12(5): 39–53.
[6] Zeng X, Ma Y, Ma L. Utilization of straw in biomass energy in China. Renewable & Sustainable Energy Reviews, 2007; 11(5): 976–987.
[7] Yin Y Z, Guo C C, Sun Y J, Wu Y X, Yu Q H, Sun Z B, Wang H Y, Yang Z Y, Ma J. Effects of rape straw retention and water and nitrogen management on population quality and yield of hybrid rice under rice-rape rotation. 2019; 33(3): 257–268. (in Chinese)
[8] Cao N, Wang J, Pang J, Hu W, Bai, Zhou Z G, Meng Y L, Wang Y H. Straw retention coupled with mineral phosphorus fertilizer for reducing phosphorus fertilizer input and improving cotton yield in coastal saline soils. Field Crops Research, 2021; 274: 108309.
[9] Wang W W, Li J C, Chen L Q, Qi H J, Liang X T. Effects of key parameters of straw chopping device on qualified rate, non-uniformity and power consumption. Int J Agric & Biol Eng, 2018; 11(1): 122–128.
[10] Liu P, He J, Li Y J, Li H W, Wang Q J, Lu C Y, Zhang Z G, Li S H. Design and experiment of double rollers maize stalk chopping device with different rotation speeds. Transactions of the CSAE, 2020; 36(14): 69–79. (in Chinese)
[11] Hu H N, Li H W, Wang Q J, He J, Lu C Y, Wang Y B, Liu P. Anti-blocking performance of ultrahigh-pressure waterjet assisted furrow opener for no-till seeder. Int J Agric & Biol Eng, 2020; 13(2): 64–70.
[12] Qin K, Cao C M, Miao Y S, Wang C Q, Fang L F, Ge J. Design and optimization of crushing and throwing device for straw returning to field and fertilizing hill-seeding machine. Transactions of the CSAE, 2020; 36(3): 1–10. (in Chinese)
[13] Zhang Z Q, He J, Li H W, Wang Q J, Ju J W, Yan X L. Design and Experiment on Straw Chopper Cum Spreader with Adjustable Spreading Device. Transactions of the CSAM, 2017; 48(9): 76–87. (in Chinese)
[14] Xu L C, Zhao S W, Wu Y H, Chen Y, Zhu J, Zhang R. Design and test of spreading device for straw returning machine. Journal of Chinese Agricultural Mechanization, 2021; 42(9): 18–24. (in Chinese)
[15] Fang M, Yu Z H, Zhang W J, Liu W F, Bie Z J, Song J B. Analysis and experiments of the movement process for the shredded material of disc knife chaff cutter. Transactions of the CSAE, 2021; 37(7): 76–84. (in Chinese)
[16] Liu P, Zhang Z Q, He J, Li H W, Wang Q J, Lu C Y, Lou S Y, Liu W Z, Cheng X P. Kinematic analysis and experiment of corn straw spreading process. Inmateh-Agricultural Engineering, 2019; 58(2): 83–92.
[17] Niu G L, Li B, Liu Y, Wang S G, Wang T, Sun X X. Design and test of vertical cotton stalk crushing and returning to the field machine. Agricultural Research in the Arid Areas, 2022; 40(1): 255–263. (in Chinese)
[18] Lisowski A, Świątek K, Klonowski J, Sypuła M, Chlebowski J, Nowakowski T, Kostyra K, Strużyk A. Movement of chopped material in the discharge spout of forage harvester with a flywheel chopping unit: Measurements using maize and numerical simulation. Biosystems Engineering, 2012; 111(4): 381–391.
[19] Chen S, Ding H, Tang Z, Zhao Y F, Ding Z, Su Z. Fluid Movement Law and Influencing Factors of Shredding on Rice Straw Briquetting Machines. Agronomy, 2022; 12(6): 1439.
[20] Sun N N, Wang X Y, Li H W, He J, Wang Q J, Wang J, Liu Z D, Wang Y B. Design and experiment of differential sawing rice straw chopper for turning to field. Transactions of the CSAE, 2019; 35(22): 267–276. (in Chinese)
[21] Liang Z, Xu L Z, De B J, Li Y M, Saeys W. Optimisation of a multi-duct cleaning device for rice combine harvesters utilising CFD and experiments. Biosystems Engineering, 2020; 190: 25–40.
[22] Wang Y B, Li H W, Hu H N, He J, Wang Q J, Lu C Y, Liu P, He D, Lin X. DEM – CFD coupling simulation and optimization of a self-suction wheat shooting device. Powder Technology, 2021; 393: 494–509.
[23] Dai F, Song X F, Zhao W Y, San Z S, Zhang F W, Zhang S L. Motion simulation and test on threshed grains in tapered threshing and transmission device for plot wheat breeding based on CFD-DEM. Int J Agric & Biol Eng, 2019; 12(1): 66–73.
[24] Visconcini A R, Andrade C M G, Costa A M S. Fluid flow simulation of industrial fixed bed mixed-flow grain dryer using k-ω SST turbulence model. Int J Agric & Biol Eng, 2021; 14(2): 226–230.
[25] Liu P, He J, Li H W, Wang Q J, Lu C Y, Lou S Y, Wang Y B, Lin H, Li H. Effects of Various Edge-Curve Types and Rotational Speeds of Disc Blades on Breaking Force and Energy Consumption in the Maize Stalk Chopping Process. Applied Engineering in Agriculture, 2021; 37(5): 951–965
[26] Maia A A G, Cavalca D F, Tomita J T, Costa F P, Bringhenti C. Evaluation of an effective and robust implicit time-integration numerical scheme for Navier-Stokes equations in a CFD solver for compressible flows. Applied Mathematics and Computation, 2022; 413: 126612.
[27] Cao L Y, Shi X H, Shi W, Pei Y W. Simulation and Analysis on Flow Field in Crashing Cavity of New-type Feed Hammer Mill. Agricultural mechanization research, 2017; 39(8): 22–26. (in Chinese)
[28] Zhang Z Q, Allen D. M, Li H W, Chen L Q, He J, Lu C Y, Zheng Z Q, Wang Q J. CFD numerical simulation and optimization of the flow fields in the chopping chamber of flail chopper. International Agricultural Engineering Journal, 2017; 26(4): 74–84.
[29] Maluta F, Buffo A, Marchisio D, Montante G, Paglianti A, Vanni M. Effect of turbulent kinetic energy dissipation rate on the prediction of droplet size distribution in stirred tanks. International Journal of Multiphase Flow, 2021; 136: 103547.
[30] Zhu G H, Peng N H, Zhang A L, Ba, S, Tang H T. Influence of installation angle of submersible mixeron salt water washing and mixing effect. Journal of Xi'an Jiaotong University, 2019; 53(7): 16–22. (in Chinese)
[31] Wang L L, Wang J. Influence of diversion chamber diameter on flocculation conditions of mechanical stirring clarifier tank. Journal of China Institute of Water Resources and Hydropower Research, 2020; 18(1): 48–53. (in Chinese)